Enabling Structural and Electrochemical Stability of 2D Antimonene for Potassium-Ion Storage with Nonflammable Electrolyte

Xiaoqiong Du,*,# Xuyun Guo,# Brais González-Tobío, David Rodríguez-San-Miguel, Pascal Bargiela, Rémi Dedryvère,* Félix Zamora,* and Valeria Nicolosi*

ABSTRACT: **Alloy-type anodes with high theoretical capacities and low working potentials are promising candidates for use in rechargeable batteries. However, their development faces significant challenges due to active material pulverization associated with large volume expansion and an unstable solid electrolyte interphase (SEI) formed with conventional electrolytes. In this study, we report a two-dimensional (2D) metallene, 2D antimonene, as anode material combined with nonflammable 1 M triethyl phosphate (TEP) and tris(2,2,2-trifluoroethyl) phosphate (TFP)-based electrolytes, achieving structural and electrochemical stability for potassium-ion storage. We disclose that the 2D antimonene develops a wrinkled morphology while retaining its structural integrity without cracking after cycling, highlighting its effectiveness in accommodating stress from large volume change. Meanwhile, TEP-based electrolyte accelerates the formation of stable anion-derived SEI, and TFP-based electrolyte produces a KF-rich SEI, effectively passivating the electrochemical interface and preventing electrolyte depletion. In potassium-ion batteries (PIBs), 2D antimonene delivers stable capacities of 486.8/492.6 mAh g^{-1} with retention of 94.6/91.4% over 200 cycles in nonflammable TEP and TFP-based electrolytes, respectively. Impressively, it obtains superior rate performance and long-term stability, maintaining a capacity of 312.3 mAh g^{-1} over 400 cycles at 0.5 A g^{-1} in the TEP system. Furthermore, the full cell was successfully demonstrated at temperatures of 50 and −20 °C. This work advances the development of 2D metallenes with nonflammable electrolytes, enabling the application of high-performance alloy-type anodes for safe PIBs.**

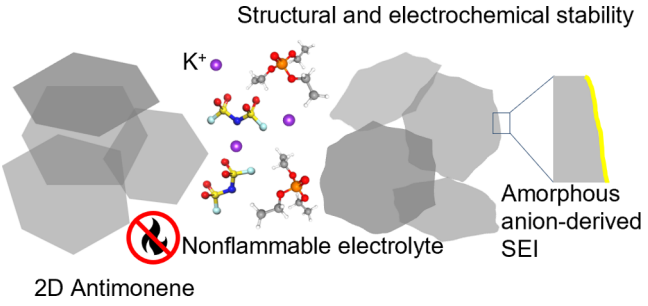

KEYWORDS: *metallene, 2D antimonene, nonflammable electrolyte, solid electrolyte interphase (SEI), potassium-ion batteries (PIBs), identical-location scanning/transmission electron microscopy (S/TEM)*

The increasing demand for portable electronics, electric vehicles, and smart grids has driven the research to explore energy storage systems with high energy density, high-level safety, and long-term sustainability.[1] Potassium-ion batteries (PIBs) are emerging as a next-generation advanced energy storage system complementary to lithium-ion batteries (LIBs) and sodium-ion batteries (SIBs) for their advantages in abundant potassium resources, low cost, and considerable energy density.[2−4] The graphite anodes, with theoretical capacity of 279 mAh g^{-1}, are approaching their performance limit in PIBs.[5] Potassium metal anodes hold significant promise for further enhancing battery energy density with the cathodes like Prussian blue analogs, layered transition metal oxides, and polyanionic compounds, while dendrite formation and low Coulombic efficiency pose serious challenges to battery safety.[6,7] Alternatively, alloy-type anodes such as antimony (Sb), bismuth (Bi), and germanium (Ge), which can accommodate multiple potassium ions and operate at low voltage platforms, deliver higher capacities than graphite, attracting considerable attention in the PIB community (Figure S1). However, these alloy anodes suffer from more severe volume expansion and structural changes than LIB and SIB cases due to the insertion/extraction of larger potassium ions.[8] This leads to the pulverization of the active particles and the cracking of solid electrolyte interphases

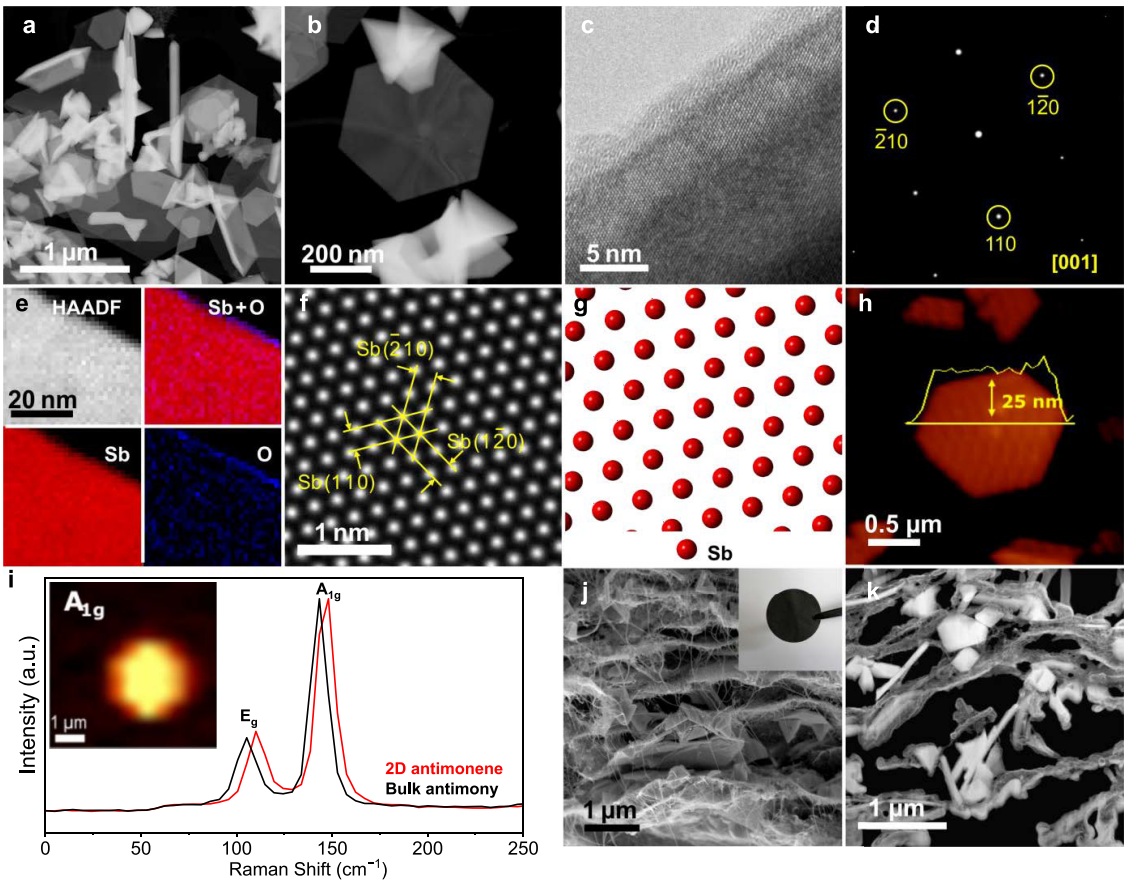

Figure 1. Characterizations of 2D antimonene and 2D antimonene/CNT electrode. (a, b) HAADF-STEM images, (c) HRTEM image, (d) SAED pattern, (e) HAADF-STEM image and corresponding EELS maps, (f) AC-ADF-STEM image of 2D antimonene and (g) corresponding atomic model; (h) AFM topography with profile (yellow line); (i) Raman spectra of 2D antimonene and bulk antimony (inset: A_{1g} Raman mapping of one antimonene flake); (j) cross-sectional SEM (inset: photo of 12 mm electrode) and (k) HAADF-STEM images of 2D antimonene/CNT electrode.

(SEIs) in traditional electrolytes, resulting in electrolyte depletion and capacity loss in the electrode.[9]

Metallenes, an emerging two-dimensional (2D) metallic materials composed of metal elements in several atomic thickness, have recently gained significant attention due to their intriguing properties such as high conductivity, fascinating structure, easily regulated electronic structures, and large exposure of metal active sites compared to bulk counterparts.[10−15] These distinctive features make 2D metallenes highly promising for a wide range of applications in energy storage and conversion, electrocatalysis, and chemical sensing.[16,17] Among them, 2D antimonene, as one member of the metallenes family, is considered a highly competitive anode candidate for PIBs due to its high theoretical capacity of 660 mAh g^{-1} achieved by accommodating three potassium ions and a low average plateau during potassium-ion storage. More importantly, the 2D structure of antimonene with reduced thickness can not only alleviate stress caused by large volume expansions but also overcome the limitations of sluggish diffusion and poor reaction kinetics,[18] further highlighting its strong potential as a high-performance anode material for PIBs.

In addition to electrode material, electrolyte is another key factor influencing electrochemical performance and plays a vital role in building SEI.[19] Compared to carbonate electrolytes, ether-based electrolytes, such as 1,2-dimethoxyethane (DME), diethylene glycol dimethyl ether (DGDME), and ethylene glycol diethyl ether (EGDEE) solvents, have been widely explored to stabilize alloy anodes by forming robust SEIs.[20−22] Such SEIs, rich in inorganic species, enabled by the high cathodic stability of ether solvents and anion-dominated decomposition, can withstand large volume changes and ensure high ionic conductivity, thereby enhancing electrochemical performance.[23] However, most of the ether-based electrolytes are highly flammable, posing significant risks to battery safety.[24] To address the flammability issue, nonflammable electrolytes based on phosphate solvents have gained increasing attention, particularly for stabilizing graphite and potassium metal anodes in PIBs.[25−29] Benefiting from their tunable solvation characteristics, the phosphate-based electrolytes effectively suppress the decomposition of the solvent molecules and promote the formation of stable passivating layers on the graphite or potassium metal anodes. Nonetheless, the development of nonflammable electrolytes for high-volume-expansion alloy anodes remains largely unexplored, particularly in low-concentration systems (1 M). The integration of 2D architectures with designed nonflammable electrolytes offers a viable strategy to resolve material pulverization problems while enhancing cycling stability and intrinsic safety. Furthermore, a comprehensive understanding of SEI evolution in alloy anodes with nonflammable electrolytes is essential for elucidating the interfacial chemistry that

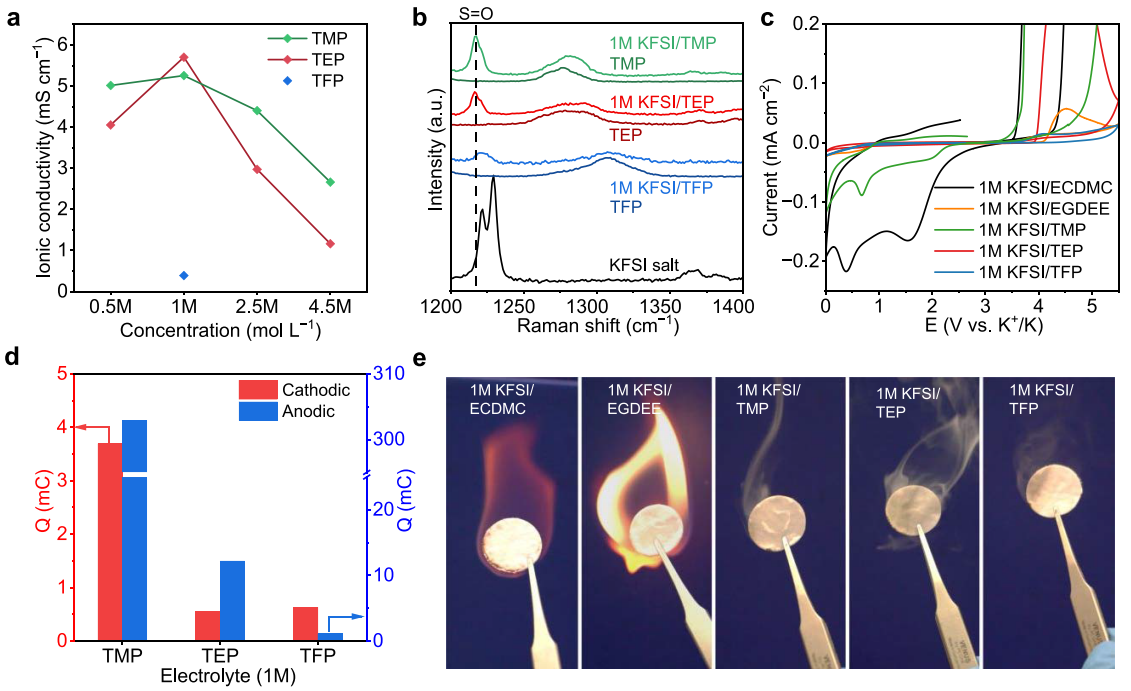

Figure 2. Characterizations of PIB electrolytes. (a) Ionic conductivity of phosphate-based electrolytes with different concentrations. (b) Raman spectra of 1 M phosphate-based electrolytes, solvents, and salt. (c) *C*−*V* curves of different electrolyte systems. (d) Integral charge during anodic and cathodic scans in 1 M KFSI/TMP, 1 M KFSI/TEP, and 1 M KFSI/TFP electrolytes. (e) Flammability tests of different electrolyte systems.

governs electrochemical performance, thus guiding the rational design of high-energy PIBs.

Herein, we employ 2D antimonene with 1 M potassium bis(fluorosulfonyl)imide (KFSI) in triethyl phosphate (TEP) and tris(2,2,2-trifluoroethyl) phosphate (TFP) nonflammable electrolytes to address the material pulverization and unstable SEI formation, demonstrating structural and electrochemical stability in PIBs. We found that 2D antimonene maintains its structural integrity by developing a wrinkled morphology, which effectively relieves stress and accommodates the large volume changes during potassium-ion storage. Meanwhile, a 3.1 nm anion-derived SEI with low-solubility forms in the TEP-based electrolyte, and a 6.7 nm KF-enriched SEI develops in the TFP-based electrolyte, functioning as protective passivation layers that enhance the interfacial stability in PIBs. As a result, 2D antimonene achieves stable electrochemical performance in PIBs, delivering 486.8 and 492.6 mAh g^{-1} capacities at 0.1 A g^{-1} with retentions of 94.6 and 91.4% over 200 cycles in 1 M KFSI/TEP and 1 M KFSI/TFP, respectively. Furthermore, it exhibits excellent rate capability and long-term stability in 1 M KFSI/TEP, retaining a capacity of 312.3 mAh g^{-1} at 0.5 A g^{-1} over 400 cycles. The perylene-3,4,9,10-tetracarboxylic dianhydride (PTCDA)||2D antimonene full cell demonstrates the outstanding capacity performance over a wide temperature range from −20 to 50 °C. This work provides valuable insights into the study of 2D metallenes and nonflammable electrolytes, opening opportunities for the development of high-performance, and safe PIBs.

RESULTS AND DISCUSSION

Nanostructure of 2D Antimonene and 2D Antimonene/CNT Electrode. 2D antimonene was prepared using a solution-phase synthesis approach and identified as the rhombohedral β-phase (PDF#00-035-0732) based on X-ray diffraction analysis (XRD, Figure S2). High-angle annular dark-field scanning transmission electron microscopy (HAADF-STEM, Figure 1a,b) and scanning electron microscopy (SEM, Figure S3) images revealed flake-like morphologies with a lateral dimension of several micrometers and well-defined flat facets. The nanostructure and single-crystal nature of 2D antimonene were confirmed by high-resolution TEM (HRTEM, Figure 1c) and selected area electron diffraction (SAED, Figure 1d) pattern. The hexagonal symmetry of the SAED pattern was indexed to the rhombohedral phase of the 2D antimonene (COD#5000214) with the [001] zone axis. A ~2 nm native oxidation layer was observed on the material surface in HRTEM and electron energy-loss spectroscopy (EELS) maps (Figure 1e), which was identified as Sb_2O_3 by X-ray photoelectron spectroscopy (XPS, Figure S4). Aberration-corrected annular dark-field STEM (AC-ADF-STEM, Figure 1f) imaging, along with the corresponding atomic model of antimony (Figure 1g), further unveiled the high-quality atomic structure of 2D antimonene with no noticeable traces of defects. Atomic force microscopy (AFM, Figure 1h) characterized the thickness of 2D antimonene, with statistical analysis revealing a thickness distribution at 25 nm (Figure S5), indicative of a few-layer antimonene structure. The chemical structure of 2D antimonene was further probed by Raman spectroscopy. Compared to bulk antimony, which exhibits two main vibrational modes at 105 cm^{-1} (E_g) and 143 cm^{-1} (A_{1g}), the Raman modes of 2D antimonene are blue-shifted to 110 and 148 cm^{-1}, respectively (Figure 1i), showing characteristic A_{1g} mode in Raman map (Figure 1i inset). This shift could attribute to the change in interlayer interactions when reducing the number of layers.[30] The 2D antimonene were incorporated with single-walled carbon nanotubes (CNTs) to prepare 2D antimonene/CNT electrode, in which CNTs functioned as both conductive agent and binder.

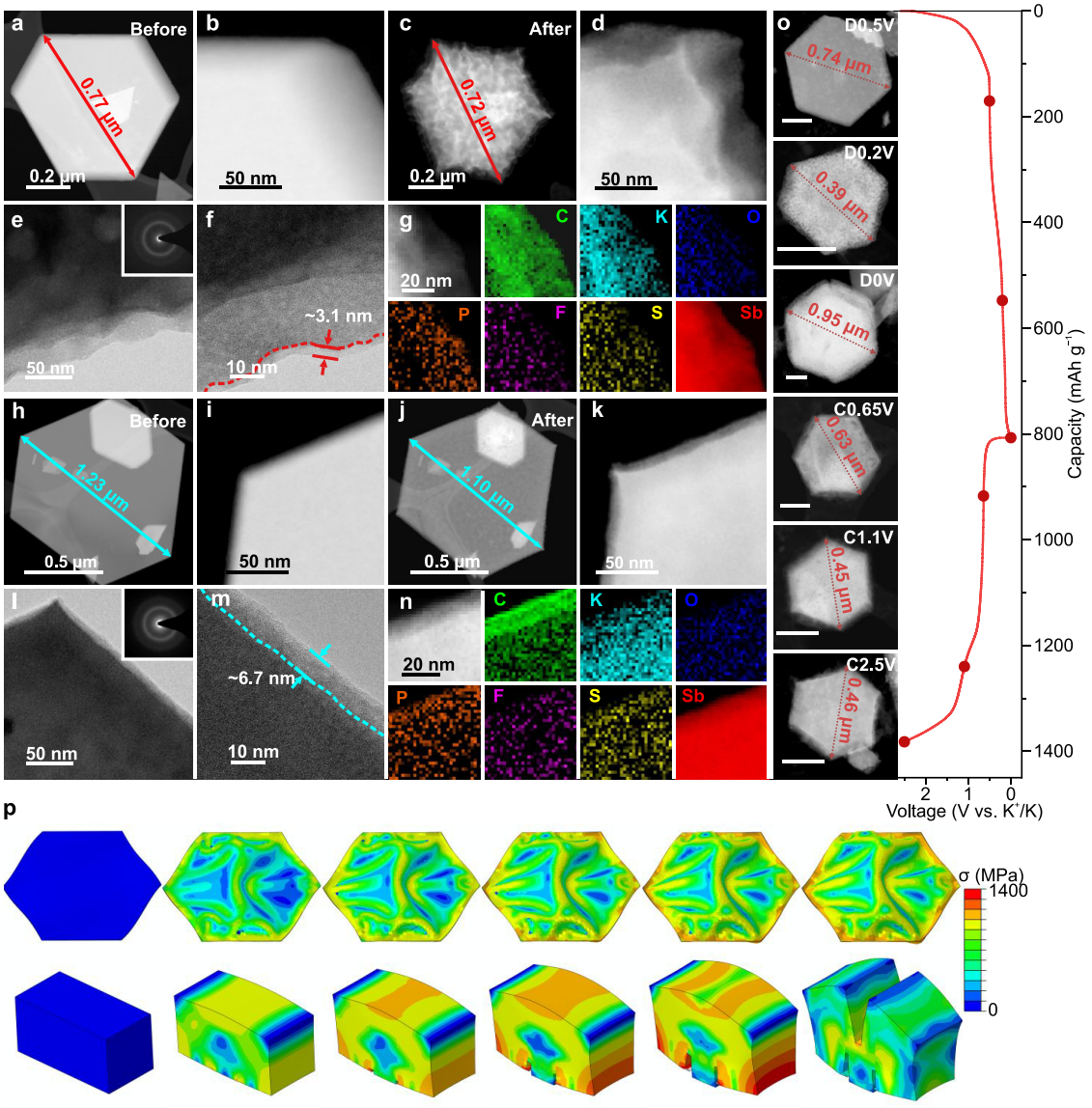

Figure 3. Identical-location S/TEM characterizations of tracked 2D antimonene with the formed SEIs and FE analysis. HAADF-STEM images of a 2D antimonene flake (a, b) before and (c, d) after cycling five times in the 1 M KFSI/TEP electrolyte; (e, f) TEM and HRTEM images, (inset, corresponding SAED), (g) HAADF-STEM and corresponding EELS maps of a 2D antimonene flake after cycling five times in the 1 M KFSI/TEP electrolyte. HAADF-STEM images of a 2D antimonene flake (h, i) before and (j, k) after cycling five times in the 1 M KFSI/TFP electrolyte; (l, m) TEM and HRTEM images, (inset, corresponding SAED), (n) HAADF-STEM and corresponding EELS maps of a 2D antimonene flake after cycling five times in the 1 M KFSI/TFP electrolyte. (o) Ex situ HAADF-STEM images (scale bar = 0.2 μm) of 2D antimonene at different voltages during the first cycle in the 1 M KFSI/TEP electrolyte, along with the corresponding discharge/charge profile. (p) FE-simulated von Mises stress (σ) distribution of 2D antimonene (top) and bulk antimony (bottom).

As observed in the SEM image (Figure 1j), the electrode displays a layered, highly porous structure, where the 2D antimonene flakes are segregated by interconnected CNT networks, as further confirmed by cross-sectional S/TEM images and EELS maps (Figures 1k and S6). Additionally, the CNTs are closely bonded to the antimonene flakes, improving the electrical conductivity of the active materials (Figure S7). This segregated architecture is believed to offer better electrolyte penetration and preserves the structural integrity of the electrode during cycling.[31]

Electrochemical Stability and Flammability of Electrolytes. To address the safety concern of electrolytes, potassium bis(fluorosulfonyl)imide (KFSI) combined with nonflammable phosphate solvents, including trimethyl phosphate (TMP), triethyl phosphate (TEP) and tris(2,2,2-trifluoroethyl) phosphate (TFP) (Figure S8), were systematically researched and compared with conventional carbonate-based and ether-based electrolytes. The ionic conductivity was initially evaluated at concentrations ranging from 0.5 to 4.5 M, as shown in Figure 2a. Except for the TFP solvent, where the maximum solubility of KFSI salt is limited to 1 M, the 1 M concentration exhibited the highest ionic conductivity among the tested electrolytes and was therefore selected for subsequent investigations. The low ionic conductivity of 1 M TFP system can be ascribed to the low polarizability of multiple fluorine substitutions in TFP solvent, which reduces electron availability on the oxygen atoms and lowers the solvating energy toward K^+ ion, as further confirmed by Raman spectroscopy.[32] In Figures 2b and S9, the S═O vibration shifts to 1222 cm^{-1} in 1 M KFSI/TFP compared with TMP and

TEP systems (1217 cm^{-1}),[33] suggesting weaker solvent coordination and stronger K^+−FSI^- interactions, which account for the lower ionic conductivity.

The electrochemical stabilities of the 1 M electrolytes were investigated using cyclic voltammetry (C−V) in a three-electrode setup with aluminum as the working electrode and potassium metal as the reference and counter electrodes. As shown in Figures 2c and S10, 1 M KFSI/TMP and 1 M KFSI in ethylene carbonate (EC) and dimethyl carbonate (DMC) with a volume ratio of 1:1 (denoted as 1 M KFSI/ECDMC) display striking current densities during the anodic scans, indicating their poor electrochemical oxidation stabilities. In contrast, 1 M KFSI/TFP demonstrates the best anodic stability, characterized by the smallest oxidation peaks (blue curve, Figure 2c), outperforming the other electrolyte systems. This can be attributed to the highly electron-withdrawing fluorine species in TFP, which lower the highest occupied molecular orbital (HOMO) of the electrolytes, thereby increasing the oxidation voltage.[34−36] In the cathodic scan, 1 M KFSI in ethylene glycol diethyl ether (denoted as 1 M KFSI/EGDEE), 1 M KFSI/TEP, and 1 M KFSI/TFP present weak current peaks, highlighting their superior electrochemical reductive stability. An analysis of the integral charge during anodic and cathodic scans for the phosphate-based electrolytes was quantified in Figure 2d. The lower oxidation and reduction charges of the 1 M KFSI/TEP and 1 M KFSI/TFP electrolytes make them promising candidates. Moreover, considering that antimony potassiation occurs below 0.85 V (Figure S11),[37] the excellent electrochemical stability against reduction in TEP and TFP systems is essential for suppressing excessive electrolyte decomposition on the active material surface and facilitating the formation of effective SEIs, as demonstrated in ether-based systems.[20,22] In addition, unlike the high flammability of commonly used carbonate- and ether-based electrolytes, phosphate-based electrolytes exhibit complete nonflammability (Figure 2e), significantly reducing the risk of fires or explosions and addressing key safety concerns. This is because the phosphates can produce PO or P radicals from partial decomposition, which act as a scavenger of H radicals in the combustion reaction, thereby terminating the chain reaction and suppressing the combustion reaction.[38]

Nanostructural Evolution of 2D Antimonene and SEI. To elucidate the volume change of 2D antimonene and the nanostructure of SEI during potassium-ion storage, we employed an identical-location tracking strategy within the S/TEM and EELS techniques, examining the same individual 2D antimonene flake before and after cycling. As shown in Figure 3a−d, the tracked 2D antimonene flake retains its overall integrity without cracking after five potassiation/depotassiation cycles in 1 M KFSI/TEP but undergoes a morphological transformation from a flat to a wrinkled structure, with its lateral dimension decreasing from 0.77 to 0.72 μm. The SAED pattern after cycling (Figure 3e inset) displays a halo feature, signifying the phase transition from a single crystal to an amorphous structure. Examination of the TEM and HRTEM images (Figure 3e,f) shows a thin, amorphous SEI layer on the antimonene surface with a thickness of around 3.1 nm. The EELS maps (Figure 3g) probe the K, P, F, and S elements, which stem from electrolyte decomposition. The identical-location S/TEM results for 1 M KFSI/TFP are shown in Figure 3h−k. Similar to the TEP case, the 2D antimonene flake shrinks from 1.23 to 1.10 μm without visible breakage. The SAED pattern also reveals an amorphous structure of antimonene after potassium alloying/dealloying (Figure 3l inset). TEM and HRTEM images show a slightly thicker SEI layer of 6.7 nm formed with this electrolyte (Figure 3l,m). The EELS maps clarify the presence of C and P elements aggregated on the surface, which probably comes from the decomposition of the electrolyte solvent (Figure 3n). Compared with TFP case, the reduced thickness of SEI in the TEP system is expected to shorten the potassium-ion diffusion pathway and facilitate ion transport, which could enhance the rate capability of PIBs. Furthermore, ex situ identical-location S/TEM (Figures 3o and S12) and finite element (FE, Figure 3p) analysis were performed to investigate the wrinkling mechanism of 2D antimonene and its advantage in accommodating large volume changes. During potassiation, 2D antimonene gradually develops small internal wrinkles with increased lattice strain (Figure S13), and the wrinkled structure remains intact without fracture upon depotassiation. The lateral dimension ratio changes from 0.97 to 1.02 during potassiation and decreases to 0.89 at the fully depotassiation state (Figure S14), demonstrating its remarkable ability to accommodate volume changes. FE analysis (Figure 3p, top) further reveals that aided by weaker interlayer interactions of 2D antimonene, the uneven stress distribution drives wrinkle formation, thus effectively releasing stress without causing cracks. In contrast, the bulk antimony fails to gradually release the stress through wrinkling, resulting in sudden cracking to relieve accumulated stress (Figure 3p, bottom), as also confirmed by HAADF-STEM observation (Figure S15).

However, the 2D antimonene maintains its original flat morphology and single-crystal phase in 1 M KFSI/TMP (Figure S16), implying an unsuccessful potassiation reaction. A ∼2.5 nm surface layer containing C, K, P, F, and S elements is observed (Figure S16d,f). In the conventional 1 M KFSI/ECDMC (Figure S17), electrochemical interface instability still causes fracture and thick SEI (∼9.3 nm), which exposes a more active antimonene surface to the electrolyte and accelerates electrolyte decomposition, ultimately leading to capacity degradation and Coulombic efficiency decline. The overall morphologies of 2D antimonene/CNT electrodes before and after cycling in PIBs with nonflammable electrolytes were also investigated using cross-sectional SEM. As shown in Figure S18, the electrodes cycled in 1 M KFSI/TEP and 1 M KFSI/TFP exhibit a slight thickness increase and retain well-preserved internal voids (Figure S18a−f), whereas the electrode cycled 1 M KFSI/TMP displays a dense structure (Figure S18g,h). These findings suggest that the 2D antimonene with nonflammable 1 M KFSI/TEP and 1 M KFSI/TFP demonstrates robust structural stability and forms effective SEIs on its surface, enabling efficient potassiation/depotassiation and preventing structural collapse of the host material.

Chemical Composition and Solubility of SEI. To further investigate the chemical composition and solubility of the SEIs formed on 2D antimonene anode with nonflammable electrolytes, we conducted XPS measurements on the rested, nonwashed, and soaked electrodes. The XPS spectra of the 2D antimonene/CNT electrode after resting for 4 h in the 1 M KFSI/TEP electrolyte are presented in Figure S19. The presence of K species can be evidenced by two K $2p_{3/2}$ and K $2p_{1/2}$ peaks at 293.1 and 295.8 eV, respectively (Figure S19a). The P $2p$ spectrum of the 2D antimonene/CNT electrode shows no evidence of TEP solvent decomposition (Figure S19b). In contrast, the S $2p$ and F $1s$ core peaks (Figure

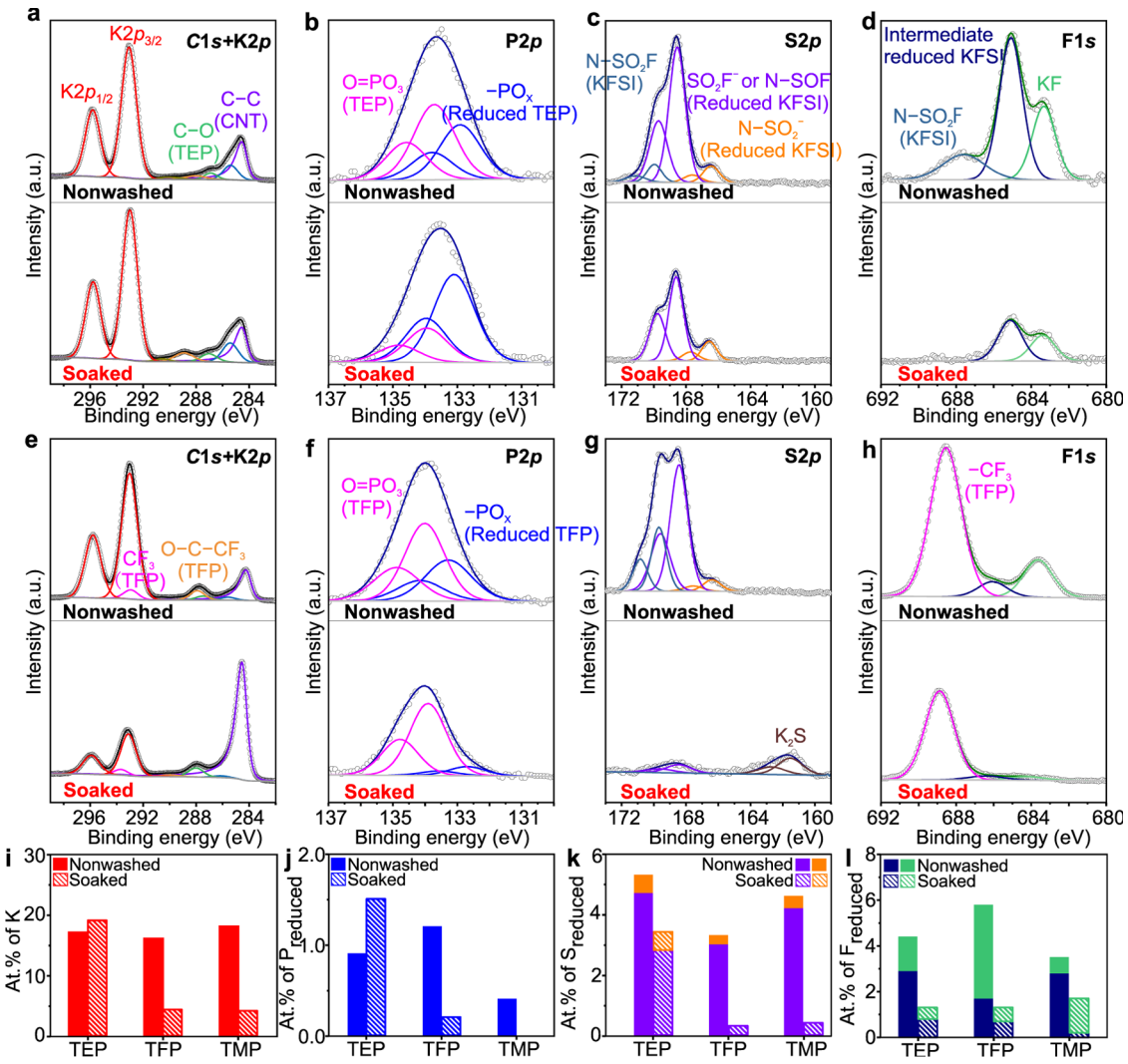

Figure 4. XPS characterization for the chemical compositions and solubility of SEIs formed in nonflammable electrolytes. Comparison of high-resolution (a) C 1*s* and K 2*p*, (b) P 2*p*, (c) S 2*p*, and (d) F 1*s* spectra of nonwashed (top) and soaked (bottom) 2D antimonene/CNT electrode after cycling five times in the 1 M KFSI/TEP electrolyte. Comparison of high-resolution (e) C 1*s* and K 2*p*, (f) P 2*p*, (g) S 2*p*, and (h) F 1*s* spectra of the nonwashed (top) and soaked (bottom) 2D antimonene/CNT electrode after cycling five times in the 1 M KFSI/TFP electrolyte. The comparison of the atomic percentage of (i) potassium element, (j) reduced phosphorus element in P 2*p*, (k) reduced sulfur element in S 2*p*, and (l) reduced fluorine element in F 1*s* (Note: The solid columns represent the nonwashed samples, while the striped columns correspond to the soaked samples, with the color matching the species in the spectra).

S19c,d) showcase the presence of reduction species derived from KFSI salt, implying that the preformed SEI layer primarily originates from spontaneous decompositions of the salt. For the nonwashed samples after five cycles, the CNT, residual solvent and K species are detected in C 1*s* and K 2*p* spectra (top part of Figures 4a,e and S20a). In P 2*p* spectra, besides the P 2*p* doublet attributed to the residual solvent (at 133.7 eV for TEP, 134.0 eV for TFP and 133.6 eV for TMP) as shown in the top part of Figures 4b,f and S20b, another set of P 2*p* doublet at lower binding energies of 132.9, 133.3, and 132.5 eV is associated with the reduction of these solvents, with phosphorus remaining in the oxygen environment. In S 2*p* spectra (top part of Figures 4c,g and S20c), aside from the KFSI peak at 170.0 eV, two S 2*p* doublets with S $2p_{3/2}$ at 168.6 and 166.4 eV are assigned to species of FSI^- anion decomposition. The first one could be due to the breakdown of the N–S bond leading to a fluorosulfite SO_2F^- anion,[39] or the breakdown of the S=O bond resulting in an N–SOF environment. The second one is probably due to the bond-cleavage of the S–F leading to an $N–SO_2^-$ environment. In the F 1*s* spectra of TEP and TMP cases (top part of Figures 4d and S20d), three components are observed at 687.6, 685.1, and 683.3 eV, attributed to the KFSI salt, an intermediate reduction product of FSI^- anion and KF, respectively. Due to the presence of a fluorine source in the TFP solvent, an additional peak at a higher binding energy of 688.5 eV (Figure 4h, top) is attributed to the $-CF_3$ group in the TFP solvent, which dominates the F 1*s* spectrum of this sample. Additionally, two distinct peaks at lower binding energies of 686.1 and 683.6 eV can be assigned to the reduction of TFP/KFSI and KF, respectively. All XPS data were quantified (Tables S1–S8) to comprehensively analyze the decomposition trends of solvent and salt in these electrolyte systems. Electrolyte decomposition in 1 M KFSI/TEP produces a high abundance of decomposed S species (Figure 4k, solid columns), corresponding to significant FSI^- anions reduction (Figure S21a) and pointing to the formation of an anion-derived SEI. Strong $K^+–FSI^-$ coordination in 1 M KFSI/TFP leads to

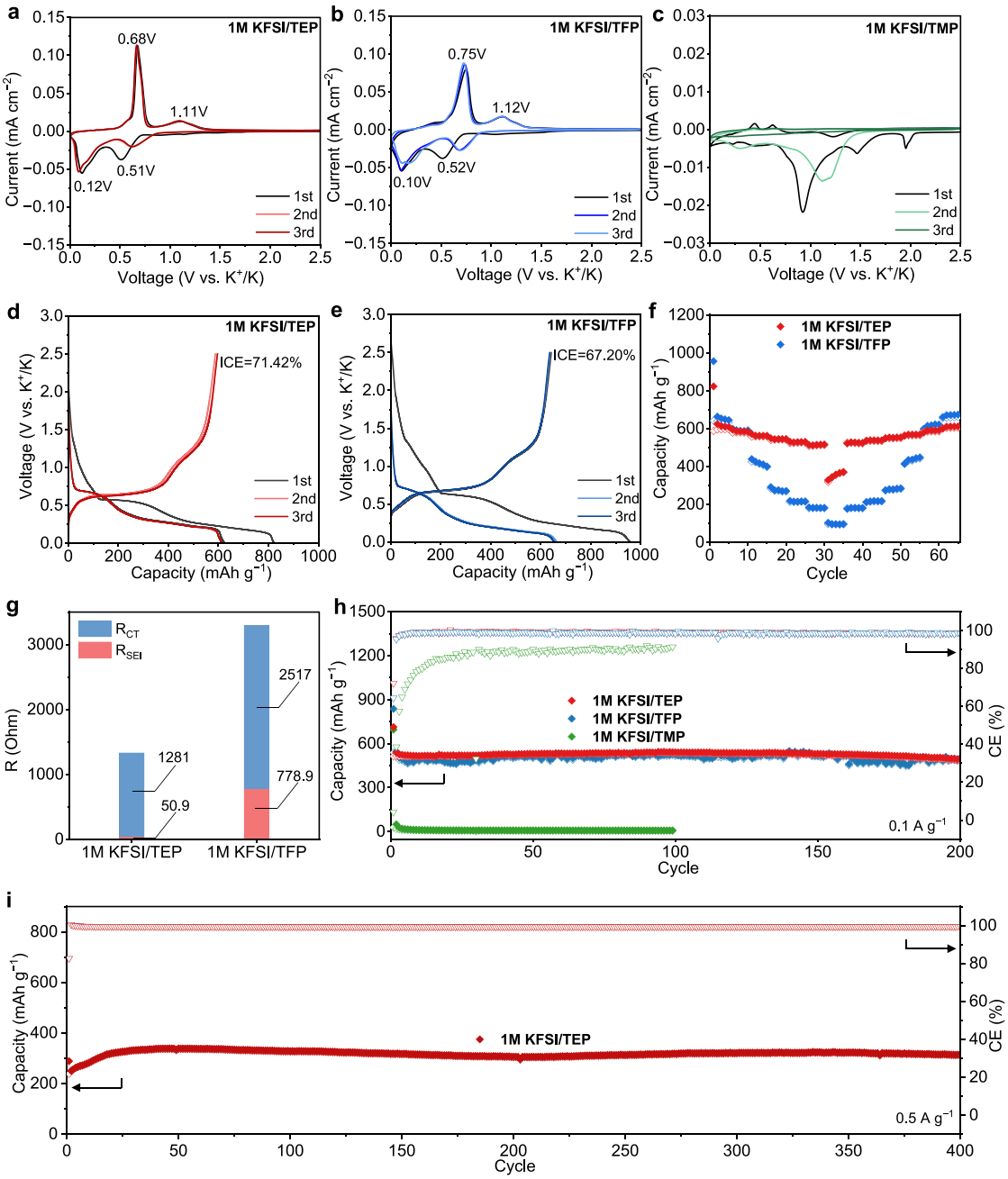

Figure 5. Electrochemical performance measurements of 2D antimonene/CNT electrode in PIBs. *C*−*V* measurements of 2D antimonene/CNT in (a) 1 M KFSI/TEP, (b) 1 M KFSI/TFP, and (c) 1 M KFSI/TMP electrolytes. Selected galvanostatic discharge/charge profiles of 2D antimonene/CNT electrode in (d) 1 M KFSI/TEP, (e) 1 M KFSI/TFP electrolytes at current densities of 0.05 A g^{-1}. (f) Rate performance at current densities increasing from 0.05, 0.1, 0.2, 0.3, 0.4, 0.5 to 1 A g^{-1} and then decreasing to 0.05 A g^{-1}. (g) The fitted R_{CT} and R_{SEI}. (h) Cyclic performance between 0 and 2.5 V at a current density of 0.1 A g^{-1}. (i) Long-term cyclic performance in 1 M KFSI/TEP between 0 and 1 V at a current density of 0.5 A g^{-1}.

deeper decomposition, yielding a high concentration of KF species (Figure 4l, solid columns) and thereby forming a KF-rich SEI (Figure S21b).

The solubility of various SEI ingredients was systematically studied by comparing the XPS spectra of the nonwashed samples with those soaked for 48 h. In the P 2*p* spectra (bottom part of Figures 4b,f and S20b), the solvent peaks persist with reduced intensity, while the KFSI peaks are absent in the S 2*p* (bottom part of Figures 4c,g and S20c) and F 1*s* (bottom part of Figures 4d and S20d) spectra, confirming the successful removal of electrolyte salt after soaking. Quantitative comparison in Figure 4i−k (striped columns) shows the TEP system retains higher percentages of K, P, and S species after soaking, indicating the low solubility of these species in 1 M KFSI/TEP. Decomposed F species also present lower solubility in the TEP system compared with the TFP system, while P species disappears in the TMP system, pointing to high solubility. Moreover, as soaking process was intended to remove soluble SEI components and salt while exposing the substrate, SEI stability can be estimated by comparing changes in the characteristic signals of the Sb and CNT alone. As shown in Figure S22, the content of the Sb element and CNT

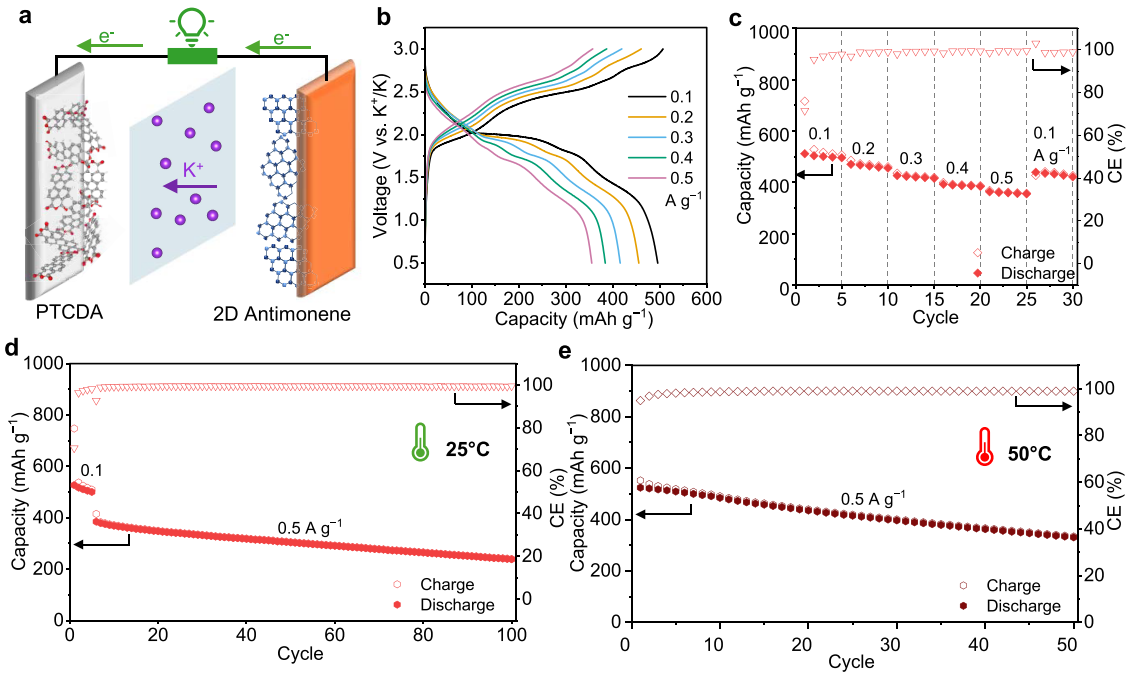

Figure 6. Electrochemical performance measurements of PTCDA||2D antimonene full cell with the 1M KFSI/TEP electrolyte. (a) Schematic illustration of the PTCDA||2D antimonene full cell. (b) Selected galvanostatic discharge/charge profiles of the full cell at current densities increasing from 0.1 to 0.5 A g^{-1} at 25 °C. (c) Rate performance of the full cell at 25 °C. (d) Cyclic performance of the full cell at 25 °C under current density of 0.5 A g^{-1}. (e) Cyclic performance of the full cell at 50 °C under current density of 0.5 A g^{-1} (Note: the capacity is calculated based on the mass of the 2D antimonene active material.).

in nonwashed and soaked electrodes in the TEP case remains almost constant, further indicating that the formed SEI has the best stability among the three. These results demonstrate that the 1 M KFSI/TEP forms a robust, low-solubility SEI layer that effectively passivates the antimonene surface and suppresses continuous electrolyte decomposition, thereby ensuring a long-term electrochemical stability.

Electrochemical Performance in PIBs. Based on the above results, structural and interfacial stability can be achieved for 2D antimonene during potassium-ion storage. Accordingly, electrochemical measurements were conducted to evaluate their performance in PIBs. As shown in Figure 5a,b, the *C*−*V* curves of 2D antimonene/CNT electrode with 1 M KFSI/TEP and 1 M KFSI/TFP electrolytes display two pairs of well-defined peaks. The cathodic peaks at ∼0.5 and ∼0.1 V can be attributed to the formation of K_xSb and K_3Sb phases during the potassium alloying processes, and two anodic peaks at ∼0.7 and ∼1.1 V correspond to their dealloying reactions.[40] Ex situ XRD and TEM (Figures S23 and S24) further unveil its crystalline-to-amorphous phase transitions: crystalline Sb → amorphous K_xSb → crystalline K_3Sb → amorphous K_xSb → amorphous Sb. In 1 M KFSI/TMP (Figure 5c), no prominent anodic peak is observed during the anodic scan, which indicates that no alloying reaction occurs between potassium and antimonene. This is consistent with the XRD patterns at the fully potassiated state (Figure S25), where unreacted Sb is still present. In the galvanostatic discharge/charge measurements (Figure 5d,e), the 2D antimonene/CNT electrode delivers high initial reversible capacities of 587.9 and 642.5 mAh g^{-1} in 1 M KFSI/TEP and 1 M KFSI/TFP at 0.05 A g^{-1}, corresponding to initial Coulombic efficiencies (ICEs) of 71.42 and 67.20%, respectively. Their K^+ diffusion coefficients were evaluated using the *C*−*V* rate (Figure S26), showing a slightly higher value in the TFP-based electrolyte (Figure S27). For 1 M KFSI/TMP, it yields a negligible reversible capacity and a low ICE of 4.14% (Figure S28), aligning with the *C*−*V* results.

The rate capabilities in 1 M KFSI/TEP and 1 M KFSI/TFP electrolytes are compared in Figure 5f. As the current density increases from 0.05 to 1 A g^{-1}, the 2D antimonene/CNT electrode in the 1 M KFSI/TEP achieves rate capacities of 597.7, 578.9, 558.8, 542.6, 527.9, 513.8, and 369.7 mAh g^{-1}, outperforming other reported anodes (Figure S29) and its TFP counterpart at higher rates, which exhibits capacities of 632.8, 585.6, 397.5, 269.3, 214.7, 180.9, and 95.9 mAh g^{-1}. Moreover, the electrode shows smaller voltage polarization at high current densities in 1 M KFSI/TEP compared to 1 M KFSI/TFP (Figure S30). Additionally, electrochemical impedance spectroscopy (EIS) was employed to investigate the kinetics of these two electrolytes. The Nyquist plots of cycled 2D antimonene/CNT electrodes in both electrolytes show two semicircles at high and medium frequencies (Figure S31a−c), corresponding to the resistances of SEI (R_{SEI}) and charge transfer (R_{CT}), respectively. The results were fitted using an equivalent circuit model (Figure S32), yielding an R_{SEI} of 50.9 Ω for the TEP case, significantly smaller than the values in the TFP-based electrolyte (778.9 Ω) (Figure 5g). Meanwhile, a lower R_{CT} is observed for the TEP-based electrolyte compared to the TFP one (1281 vs. 2517 Ω), reflecting more efficient charge transfer in 1 M KFSI/TEP. The high ionic conductivity, facile charge-transfer kinetics, and thinner low-resistance SEI associated with the 1 M KFSI/TEP electrolyte collectively contribute to its enhanced rate performance. The cyclic performances of these electrolytes are shown in Figure 5h. The 2D antimonene/CNT electrodes achieve stable capacities of 486.8 and 492.6 mAh g^{-1} over 200 cycles at 0.1 A g^{-1}, with capacity retentions of 94.6 and 91.4% in 1 M KFSI/TEP and 1

M KFSI/TFP, respectively, offering performance comparable to leading conversion- and intercalation-type anodes in PIBs.[41,42] The long-term cyclic stability of the TEP-based electrolyte was further evaluated at 0.5 A g^{-1} between 0 and 1 V. Remarkably, the 2D antimonene/CNT electrode in 1 M KFSI/TEP maintains an outstanding capacity retention of 312.3 mAh g^{-1} over 400 cycles, as observed in Figure 5i. It demonstrates the promising application of stabilizing antimony-based alloy anode in PIBs using the 1 M nonflammable electrolyte, achieving performance comparable or superior to previously reported high-concentration and flammable electrolytes (Table S9). The electrochemical performance of 2D antimonene/CNT in the conventional carbonated-based electrolyte (1 M KFSI/ECDMC) is also compared in Figure S33. It presents a rapid decrease in capacity and Coulombic efficiency after around 25 cycles, implying unstable electrolyte decomposition and host material breakdown, as observed in Figure S17d. Additionally, the inferior cycling performance of microsized antimony electrodes (Figures S34 and S35) in 1 M KFSI/TEP and 1 M KFSI/TFP highlights the advantages of the 2D antimonene material toward potassium-ion storage. It is believed that the 2D structure of antimonene and the formed stable anion-derived SEIs synergistically contribute to maintaining structural and electrochemical stability, thus enabling stable potassium-ion storage.

The full cell comprising the 2D antimonene/CNT anode and perylene-3,4,9,10-tetracarboxylic dianhydride (PTCDA) cathode was demonstrated with the 1 M KFSI/TEP electrolyte (Figure 6a). As presented in Figure S36, the PTCDA cathode was prepared and tested in PIBs, exhibiting a stable capacity of 117.2 mAh g^{-1} after 60 cycles at 0.05 A g^{-1}. The PTCDA||2D antimonene full cell demonstrated excellent rate performance, delivering discharge capacities of 511.5, 470.1, 426.3, 392.6, and 363.1 mAh g^{-1} at current densities of 0.1, 0.2, 0.3, 0.4 to 0.5 A g^{-1} (Figure 6b,c). The cycling performance of the full cell is shown in Figure 6d, which maintains a reversible capacity of 238.4 mAh g^{-1} after 100 cycles under a high current density of 0.5 A g^{-1}. Additionally, the high-temperature electrochemical performance of PTCDA||2D antimonene full cell with nonflammable 1 M KFSI/TEP was evaluated at 50 °C. As depicted in Figure 6e, the full cell retained a decent capacity of 330.7 mAh g^{-1} with an average CE of ~99% over 50 cycles under 0.5 A g^{-1} at 50 °C. Even when the temperature drops to −20 °C, the full cell operated effectively, achieving a high initial capacity of 444.03 mAh g^{-1} (Figure S37) under 0.1 A g^{-1}. Overall, the full cell results show promising practical application potential of 2D antimonene and nonflammable 1 M KFSI/TEP electrolytes in PIBs.

CONCLUSIONS

In summary, 2D antimonene anodes with nonflammable phosphate-based electrolytes were systematically investigated in PIBs. Identical-location S/TEM revealed that 2D antimonene maintains excellent structural stability by developing a wrinkled morphology, with the formation of 3.1 and 6.7 nm SEIs in the 1 M KFSI/TEP and 1 M KFSI/TFP electrolytes, respectively. FE analysis further demonstrated that uneven stress induces wrinkle formation, which effectively relieves stress without causing cracks. The chemical compositions and solubility of SEIs were further examined through XPS analysis. In the TEP case, significant reduction of FSI^- anion forms a low-solubility anion-derived SEI, while in the TFP system, deeper decomposition produces a high concentration of F species, resulting in a KF-rich SEI. Benefiting from the 2D structure and effective SEI formation, we achieved stable capacities of 486.8 and 492.6 mAh g^{-1} at 0.1 A g^{-1} with retentions of 94.6 and 91.4% over 200 cycles in nonflammable 1 M KFSI/TEP and 1 M KFSI/TFP, respectively. Moreover, 1 M KFSI/TEP enabled outstanding rate capability and long-term cycling stability, obtaining a capacity of 312.3 mAh g^{-1} over 400 cycles at 0.5 A g^{-1}. The successful demonstration of the PTCDA||2D antimonene full cell across 50 and −20 °C temperatures further highlights the practical application potential of 2D metallenes and low-concentration, nonflammable 1 M KFSI/TEP electrolytes for next-generation PIBs.

MATERIALS AND METHODS

2D Antimonene Synthesis. The synthesis of 2D antimonene was conducted using a modified procedure adapted from previous reports.[43,44] The process involved two main steps: preparation of the $SbCl_3$-DDT precursor and synthesis of 2D antimonene, both performed under an argon atmosphere using standard Schlenk techniques.

For $SbCl_3$-DDT precursor preparation, 4 mmol of $SbCl_3$, (0.912 g, antimony(III) chloride, Sigma-Aldrich, ≥99.95%), 4.0 mL of DDT (1-dodecanethiol, Sigma-Aldrich, ≥98%), and 6.0 mL of ODE (octadecene, Sigma-Aldrich, 70%) were added into a 50 mL three-neck flask. The mixture was degassed under vacuum at 110 °C for 2 h using a heating mantle (Fibroman HT-W), followed by argon purging for 15 min. The mixture was then heated to 150 °C under argon and maintained at this temperature until the reaction between $SbCl_3$ and DDT was complete, as indicated by a visible color change from transparent to yellowish (typically within 2 h).

For 2D antimonene synthesis, 0.5 mL of OA (oleylamine, Sigma-Aldrich, 70%) and 4.0 mL of ODE were added to another 50 mL three-neck flask. The mixture was degassed under vacuum at 110 °C for 30 min and purged with argon for 15 min. The temperature was then raised to 300 °C under argon. Once the target temperature was reached, 1 mL of the $SbCl_3$-DDT precursor (preheated to 60 °C) was rapidly injected into the flask. The reaction was quenched by immediately removing the flask from the heating mantle and allowing it to cool to room temperature. The product was isolated by centrifugation using an MPW 350R centrifuge at 4500 rpm (3300 rcf) for 5 min. The resulting 2D antimonene were washed three times with chloroform ($CHCl_3$, Thermo Scientific Chemicals, HPLC grade, ≥99.5%) under the same centrifugation conditions, maintaining the temperature at 5 °C to minimize chloroform evaporation. Each washing step involved redispersing the precipitate in 10 mL of chloroform, followed by shaking in a vortex until complete resuspension before centrifugation. Finally, the product was dried under vacuum at 80 °C overnight.

Electrode Preparation. The 2D antimonene/CNT electrode was prepared by vacuum filtrating a dispersion of 2D antimonene and carbon nanotubes (CNTs, P3-SWNT, Carbon Solutions, Inc.), with a mass ratio of active material to CNTs of 80:20. No other conductive carbon or binder was used in the electrode. A CNT dispersion (0.1 mg mL^{-1}) was prepared by probe sonication of 8 mg of CNT and 80 mL of isopropyl alcohol (IPA, Sigma-Aldrich) for 30 min using a Fisherbrand Ultrasonic Dismembrator (500 W, 60% amplitude), followed by bath sonication (Fisherbrand FB11207, 37% frequency, 100% power) for an additional 30 min. The temperature during probe sonication was controlled at 4 °C using a cooling system. The 2D antimonene dispersion (0.5 mg mL^{-1}) was prepared by mixing 10 mg of 2D antimonene with 20 mL of IPA, followed by bath sonication (Fisherbrand FB11207, 37% frequency, 100% power) for 30 min. To prepare the 2D antimonene/CNT electrode, 25 mL of prepared CNT dispersion was added to the antimonene and IPA dispersion. The mixture was then further bath-sonicated for 90 min. The temperature during bath sonication was controlled between 20 and 25 °C using ice. The mixed homogeneous dispersion was vacuum filtrated using a Celgard 2320 separator as the filtration membrane. After vacuum

filtration, the electrode was dried in a Büchi glass oven at 80 °C under vacuum for 12 h. The microsized antimony electrode was prepared by hand grinding 70 wt % antimony (Sigma-Aldrich, ∼100 mesh, 99.5%), 20 wt % carbon black (super P, MTI Corporation), and 10 wt % carboxymethyl cellulose (CMC, MTI Corporation). The slurry was then cast onto a Cu current collector and dried in a Büchi glass oven at 80 °C under vacuum for 12 h. The perylene-3,4,9,10-tetracarboxylic dianhydride (PTCDA, 97%, Sigma-Aldrich) cathode was prepared by hand-grinding the slurry containing 70 wt % active material, 20 wt % super P (MTI Corporation), and 10 wt % of CNT/PVDF (Tuball CNT solution, 0.2%CNT, 2%PVDF). The slurry was then cast onto an Al current collector and dried in a Büchi glass oven at 80 °C under vacuum for 12 h. In half-cell and full-cell tests, the anode and cathode active materials had mass loadings of around 1.0 and 7.0 mg cm^{-2}, respectively.

Electrolyte Preparation. Potassium bis(fluorosulfonyl)imide (KFSI, >99.5%) and tris(2,2,2-trifluoroethyl) phosphate (TFP, >96.0%) were purchased from Tokyo Chemical Industry (TCI EUROPE N.V.). Triethyl phosphate (TEP, ≥99.8%), trimethyl phosphate (TMP, ≥99%), ethylene carbonate (EC, ≥99%), and dimethyl carbonate (DMC, ≥99%) were bought from Sigma-Aldrich. Ethylene glycol diethyl ether (EGDEE, ≥99%) was ordered from Thermo Scientific Chemicals. The 1 M KFSI/TEP electrolyte was prepared by adding 1 mL of TEP solvent to 1 mmol of KFSI salt and stirring the mixture until it became transparent. Electrolytes including 1 M KFSI/TFP, 1 M KFSI/TMP, 1 M KFSI/ECDMC (volume ratio of EC to DMC of 1:1), 1 M KFSI/EGDEE, and other concentrations were prepared using the same method.

Electrochemical Measurement. The standard CR2032 coin cells were assembled in an Ar-filled glovebox (MBRAUN, O_2 < 0.1 ppm, H_2O < 0.1 ppm), using potassium metal as the reference/counter electrode and the 2D antimonene/CNT electrode as working electrode. Two stainless-steel spacers (0.5 mm) were used for battery assembly: one on the potassium metal side and the other one on the 2D antimonene/CNT electrode side. A piece of glass fiber (Whatman, GF/D) was added as the separator. The electrolyte volume for each coin cell was 100 μL. The cell was rested for 4 h before testing. Galvanostatic charge/discharge measurements were performed on a battery cycling system (LAND, Wuhan LAND Electronics Co., Ltd.) at 25 °C. The electrochemical impedance spectroscopy (EIS) measurements were performed using a VMP-300 Potentiostat, covering frequency ranges of 100 kHz to 1 Hz for electrolytes and 100 kHz to 10 mHz for electrodes, with AC voltage amplitudes of 5 and 10 mV, respectively. The ionic conductivity was calculated according to the equation: $\sigma = \frac{d}{AR}$, where σ is the ionic conductivity, d is the thickness of the separator, A represents the area of the stainless-steel electrode, and R is the bulk resistance of the cell with different electrolytes. Cyclic voltammetry ($C-V$) measurements of the electrolytes were conducted using a VMP-300 Potentiostat (BioLogic) in a Swagelok three-electrode cell, with a glass carbon current collector and an aluminum working electrode and potassium metal counter and reference electrodes under a scan rate of 10 mV s^{-1}. $C-V$ measurements of the 2D antimonene/CNT electrodes were collected using the BCS-805 battery cycler (BioLogic). The flammability tests were conducted in a fume hood by igniting a Whatman GF/D separator soaked with 200 μL of electrolyte. For assembling the full cell, the PTCDA cathode was precycled five times at 0.05 A g^{-1} in a 1 M KFSI/TEP electrolyte. The full cell was then assembled in glovebox using the precycled PTCDA electrode and a fresh 2D antimonene/CNT electrode with an N/P ratio of 1.04. A piece of Whatman GF/D separator soaked with 100 μL of electrolyte was used. The electrochemical performance of the full cell at different temperatures was tested using VMP-300 Potentiostat (BioLogic) in a climate chamber (aralab, TESTA_E).

Material Characterization. X-ray diffraction (XRD) data were collected using a Bruker D8 Discover X-ray diffractometer (40 kV and 40 mA) with a Cu target. The electrode samples for ex situ XRD analysis were prepared by cycling the Swagelok-type cells at different voltages with a current density of 0.1 A g^{-1} and then disassembled and sealed with Kapton tape in the glovebox. Scanning electron microscopy (SEM) images were obtained using a Zeiss Ultra SEM with a Gemini column, employing an in-lens secondary electron detector at an acceleration voltage of 5 kV. The cycled electrode for SEM imaging was prepared by cycling the electrodes five times at a current density of 0.1 mA g^{-1}, followed by disassembling the cells in the glovebox. To preserve the original structures, the electrodes were not washed. Transmission electron microscopy (TEM) and scanning TEM (STEM) were performed using an uncorrected FEI Titan 80-300 with a Schottky field-emission source operated at 300 kV. Electron energy-loss spectroscopy (EELS) maps were acquired using a Quantum Gatan Imaging Filter (GIF) detector with an energy dispersion of 0.5 eV per channel. Aberration-corrected annular dark-field STEM (AC-ADF-STEM) characterizations were performed using a Nion UltraSTEM 200 microscope equipped with a cold field-emission gun, a quadrupole-octupole type probe corrector, a Bruker Quantax EDS detector, and a Gatan Enfinium EELS detector. The microscope was operated at 200 kV with a 27 mrad convergence semiangle. The collection semiangle for ADF was 46−200 mrad. The cross-sectional S/TEM sample was prepared by using a gallium source DualBeam system (FIB, Zeiss Auriga) equipped with a platinum deposition cartridge and a nanomanipulator (Kleindiek Nanotechnik). The final thinning processes were performed with a 15 kV ion beam to minimize ion beam damage, resulting in a final lamella thickness of less than 100 nm. For identical-location S/TEM of the cycled electrodes, the 2D antimonene samples were first dispersed onto a Cu grid with asymmetrical marks, and at least eight flakes on the grid were selected and examined before being assembled into the cells. The examined Cu grid was then incorporated into a coin cell with the 2D antimonene/CNT electrode and cycled five times at 0.1 A g^{-1}. After cycling, the Cu grid was taken out by disassembling the cell in the glovebox, washing multiple times with the corresponding electrolyte solvent to remove residual electrolyte salt, and then drying inside the glovebox. Geometric phase analysis (GPA) was achieved with the Strain++ software written by Jonathan Peters (http://jjppeters.github.io/Strainpp/). Atomic force microscopy (AFM) measurements were carried out using a Cervantes Fullmode AFM from Nanotec Electronica SL. Contact mode was used to acquire all the topographies shown in this work to avoid possible artifacts in the flake thickness measurements. PPP-NCHR cantilevers with a nominal spring constant of 42 N m^{-1} and tip radius of less than 7 nm were employed. Low forces on the order of 1 nN were used for imaging to ensure that the tip would not deform the flakes. Raman spectroscopy of 2D antimonene was carried out on a confocal Raman microscope (WiTec α 300R), with laser excitation at 532 nm and a Zeiss 100× objective lens (NA = 0.9). The incident laser power was 0.5 mW. The optical diffraction resolution was about 200 nm laterally and 500 nm vertically. Raman spectral maps were acquired by adjusting the laser power to 0.2 mW and scanning a 10 × 10 μm area (30 lines, 30 points/line) at a scan rate of 4.6 s/line with an integration time of 0.5 s. The Raman map was then generated by integrating the counts of the characteristic A_{1g} Raman mode in the range of 130−170 cm^{-1}. The bulk antimony for Raman characterization was purchased from Smart Elements (99.9999%, purity crystalline pieces). Raman spectroscopy of electrolytes was carried out on Witec α 300R system equipped with a 20× objective lens and a 532 nm laser, with the laser power of 3.2 mW. Electrolytes, solvents, and salt were sealed in glass capillaries using wax in the glovebox. X-ray photoelectron spectroscopy (XPS) measurements were performed using a Thermo Scientific ESCALAB 250Xi+ spectrometer with focused monochromatized Al K_α radiation ($h\nu$ = 1486.6 eV). The spectrometer is equipped with a dry argon glovebox to maintain the samples under an inert atmosphere during all times from their preparation to their analysis. The high-resolution XPS spectra were recorded with a pass energy of 20 eV and a spot size of 650 μm. The analysis was conducted with standard charge compensation, and the chamber pressure was maintained at 2 × 10^{-7} mbar when the compensation was on (6 × 10^{-9} mbar when the compensation and the X-rays were off). The binding energy scale was calibrated using the C 1s peak of carbon nanotubes at 284.5 eV. Data fitting and analysis were performed using

CasaXPS software, applying the relative sensitivity factor (RSF) from the ESCALAB database. The cycled electrodes for XPS analysis were run five cycles at 0.1 A g^{-1}, then disassembled in the glovebox. The rested (rested for 4 h) and nonwashed samples were prepared directly from the disassembled cells. Soaked electrodes were prepared using the same cycling protocol; however, the cycled electrodes were soaked in 3 mL of each electrolyte solvent (*i.e.*, TEP for the 1 M KFSI/TEP system, TFP for the 1 M KFSI/TFP system, and TMP for the 1 M KFSI/TMP system) for 48 h to remove residual salt and dissolve the soluble SEI.

Finite Element Analysis. The numerical simulations were carried out using an Abaqus 2022. Two three-dimensional models were constructed: 2D antimonene, simplified as a regular hexagon with a diagonal length of 1 μm and a thickness of 25 nm, where buckling of the nanosheets was considered; 3D bulk antimony, simplified as a rectangular block ($1 \times 2 \times 1$ μm), where fracture behavior was considered. In the simulations, ion concentration gradients were not included, and the potassiation concentration is normalized from 0 to 1 left to right. Instead, an approach analogous to thermal expansion was applied by imposing an expansion strain on both models. The resulting internal expansion forces led to structural responses, such as wrinkling in 2D antimonene and crack propagation in bulk antimony.

ASSOCIATED CONTENT

Supporting Information

Comparison of anode materials for PIB; XRD, SEM and AFM statistics of 2D antimonene; XPS, cross-sectional TEM and top-view SEM of electrode; molecular structure of the phosphate-based solvents; Raman spectra and $C-V$ curves of electrolytes; ex situ STEM, Lattice strain analysis, lateral dimension change ratio, STEM images of cycled bulk antimony; additional S/TEM characterizations of antimonene; additional XPS spectra; comparison of atomic percentages; ex situ XRD and phase transition; HRTEM at different discharge and charge states; additional electrochemical performance with different electrolytes; EIS measurements; $C-V$ rates and diffusion coefficients; comparative analysis of rate performance; SEM and electrochemical performance of microsized antimony and PTCDA electrode; full-cell performance at −20 °C; XPS quantitative analysis tables; and comparison tables of Sb-based anodes in PIBs (PDF)

AUTHOR INFORMATION

Corresponding Authors

Xiaoqiong Du − *CRANN and AMBER research centers, Trinity College Dublin, Dublin 2, Dublin, Ireland; School of Chemistry, Trinity College Dublin, Dublin 2, Dublin, Ireland*; Email: xidu@tcd.ie

Rémi Dedryvère − *Réseau sur le Stockage Electrochimique de l'Energie (RS2E), CNRS, Paris FR 3459, France; IPREM, CNRS, Université de Pau & Pays Adour, E2S-UPPA, Pau 64000, France*; orcid.org/0000-0001-5125-640X; Email: remi.dedryvere@univ-pau.fr

Félix Zamora − *Departamento de Química Inorgánica, Institute for Advanced Research in Chemical Sciences (IAdChem), and Condensed Matter Physics Center (IFIMAC), Universidad Autónoma de Madrid, Madrid 28049, Spain*; orcid.org/0000-0001-7529-5120; Email: felix.zamora@uam.es

Valeria Nicolosi − *CRANN and AMBER research centers, Trinity College Dublin, Dublin 2, Dublin, Ireland; School of Chemistry, Trinity College Dublin, Dublin 2, Dublin, Ireland*; orcid.org/0000-0002-7637-4813; Email: NICOLOV@tcd.ie

Authors

Xuyun Guo − *CRANN and AMBER research centers, Trinity College Dublin, Dublin 2, Dublin, Ireland; School of Chemistry, Trinity College Dublin, Dublin 2, Dublin, Ireland*

Brais González-Tobío − *Departamento de Química Inorgánica, Institute for Advanced Research in Chemical Sciences (IAdChem), and Condensed Matter Physics Center (IFIMAC), Universidad Autónoma de Madrid, Madrid 28049, Spain*

David Rodríguez-San-Miguel − *Departamento de Química Inorgánica, Institute for Advanced Research in Chemical Sciences (IAdChem), and Condensed Matter Physics Center (IFIMAC), Universidad Autónoma de Madrid, Madrid 28049, Spain*; orcid.org/0000-0002-1476-2175

Pascal Bargiela − *Réseau sur le Stockage Electrochimique de l'Energie (RS2E), CNRS, Paris FR 3459, France; IPREM, CNRS, Université de Pau & Pays Adour, E2S-UPPA, Pau 64000, France*

X.D. and X.G. contributed equally to this work.

Notes

The authors declare no competing financial interest.

ACKNOWLEDGMENTS

X.D. acknowledges Marie Skłodowska-Curie Grant Agreement No. 101107396. X.G. and V.N. wish to thank the Advanced Microscopy Laboratory (AML) in CRANN for the provision of their facilities. X.D., X.G., and V.N. wish to thank the support of the Research Ireland-funded AMBER research center, and the Research Ireland Frontiers for the Future award (Grant Nos. 12/RC/2278_P2 and 20/FFP-A/8950, respectively). X.D. and V.N. acknowledge Shenzhen Huasuan Technology Co. Ltd. for providing the simulation platform. B.G.-T. acknowledges the financial support by the "Ayuda para Contratos Predoctorales para la Formación de Doctores" program of MICINN (PRE2020-093162). B.G.-T., D.R.-S.-M., and F.Z. wish to thank the support of the Spanish MINECO (projects PID2022-138908NB-C31 and "María de Maeztu" Programme for Units of Excellence in R&D CEX2023-001316-M), and the support from the "(MAD2D-CM)-UAM" project funded by Comunidad de Madrid, by the Recovery, Transformation and Resilience Plan, and by NextGenerationEU from the European Union. P.B. and R.D. acknowledge the French National Research Agency (ANR) for its support through the Labex STORE-EX project (ANR-10LABX-76-01).

REFERENCES

(1) Titirici, M.; Johansson, P.; Ribadeneyra, M. C.; Au, H.; Innocenti, A.; Passerini, S.; Petavratzi, E.; Lusty, P.; Tidblad, A. A.; Naylor, A. J.; et al. 2024 roadmap for sustainable batteries. *J. Phys. Energy* **2024**, *6* (4), No. 041502.

(2) Hosaka, T.; Kubota, K.; Hameed, A. S.; Komaba, S. Research Development on K-Ion Batteries. *Chem. Rev.* **2020**, *120* (14), 6358−6466.

(3) Li, X.; Wang, Y.; Wu, J.; Tong, L.; Wang, S.; Li, X.; Li, C.; Wang, M.; Li, M.; Fan, W.; et al. Engineering contact curved interface with high-electronic-state active sites for high-performance potassium-ion batteries. *Proc. Natl. Acad. Sci. U. S. A.* **2023**, *120* (52), No. e2307477120.
(4) Du, X.; Zhang, B. Robust solid electrolyte interphases in localized high concentration electrolytes boosting black phosphorus anode for potassium-ion batteries. *ACS Nano* **2021**, *15* (10), 16851−16860.
(5) Wang, D.; Du, X.; Zhang, B. Solvent Molecular Design to Regulate the Intercalation Behavior in Ether Electrolyte for Stable Graphite Anodes in Potassium-Ion Batteries. *Small Struct.* **2022**, *3* (10), No. 2200078.
(6) Wang, L.; Zhang, S.; Li, N.; Chen, J.; Chen, Y.; Zhang, Z.; Tan, L.; Niu, X.; Yang, Y.; Zhang, J.; et al. Prospects and Challenges of Practical Nonaqueous Potassium-Ion Batteries. *Adv. Funct. Mater.* **2024**, *34* (49), No. 2408965.
(7) Li, M.; Wang, C.; Wang, C.; Lyu, Y.; Wang, J.; Xia, S.; Mao, J.; Guo, Z. 10 Years Development of Potassium-Ion Batteries. *Adv. Mater.* **2025**, No. 2416717.
(8) Ma, M.; Chong, S.; Yao, K.; Liu, H. K.; Dou, S. X.; Huang, W. Advanced anode materials for potassium batteries: Sorting out opportunities and challenges by potassium storage mechanisms. *Matter* **2023**, *6* (10), 3220−3273.
(9) Wang, H.; Zhai, D.; Kang, F. Solid electrolyte interphase (SEI) in potassium ion batteries. *Energy Environ. Sci.* **2020**, *13* (12), 4583−4608.
(10) Kochat, V.; Samanta, A.; Zhang, Y.; Bhowmick, S.; Manimunda, P.; Asif, S. A. S.; Stender, A. S.; Vajtai, R.; Singh, A. K.; Tiwary, C. S.; Ajayan, P. M. Atomically thin gallium layers from solid-melt exfoliation. *Sci. Adv.* **2018**, *4* (3), No. e1701373.
(11) Gou, J.; Bai, H.; Zhang, X.; Huang, Y. L.; Duan, S.; Ariando, A.; Yang, S. A.; Chen, L.; Lu, Y.; Wee, A. T. S. Two-dimensional ferroelectricity in a single-element bismuth monolayer. *Nature* **2023**, *617* (7959), 67−72.
(12) Cui, J.; Daboczi, M.; Regue, M.; Chin, Y. C.; Pagano, K.; Zhang, J.; Isaacs, M. A.; Kerherve, G.; Mornto, A.; West, J.; et al. 2D bismuthene as a functional interlayer between BiVO4 and NiFeOOH for enhanced oxygen-evolution photoanodes. *Adv. Funct. Mater.* **2022**, *32* (44), No. 2207136.
(13) Tian, W.; Zhang, S.; Huo, C.; Zhu, D.; Li, Q.; Wang, L.; Ren, X.; Xie, L.; Guo, S.; Chu, P. K.; et al. Few-layer antimonene: anisotropic expansion and reversible crystalline-phase evolution enable large-capacity and long-life Na-ion batteries. *ACS Nano* **2018**, *12* (2), 1887−1893.
(14) Martínez-Periñán, E.; Down, M. P.; Gibaja, C.; Lorenzo, E.; Zamora, F.; Banks, C. E. Antimonene: a novel 2D nanomaterial for supercapacitor applications. *Adv. Energy Mater.* **2018**, *8* (11), No. 1702606.
(15) Chen, W.; Liu, C.; Ji, X.; Joseph, J.; Tang, Z.; Ouyang, J.; Xiao, Y.; Kong, N.; Joshi, N.; Farokhzad, O. C.; et al. Stanene-based nanosheets for β-elemene delivery and ultrasound-mediated combination cancer therapy. *Angew. Chem., Int. Ed.* **2021**, *60* (13), 7155−7164.
(16) Liu, Y.; Dinh, K. N.; Dai, Z.; Yan, Q. Metallenes: Recent advances and opportunities in energy storage and conversion applications. *ACS Mater. Lett.* **2020**, *2* (9), 1148−1172.
(17) Beladi-Mousavi, S. M.; Pumera, M. 2D-Pnictogens: alloy-based anode battery materials with ultrahigh cycling stability. *Chem. Soc. Rev.* **2018**, *47* (18), 6964−6989.
(18) Carrasco, J. A.; Congost-Escoin, P.; Assebban, M.; Abellán, G. Antimonene: a tuneable post-graphene material for advanced applications in optoelectronics, catalysis, energy and biomedicine. *Chem. Soc. Rev.* **2023**, *52* (4), 1288−1330.
(19) Wan, H.; Xu, J.; Wang, C. Designing electrolytes and interphases for high-energy lithium batteries. *Nat. Rev. Chem.* **2024**, *8* (1), 30−44.
(20) Zhou, L.; Cao, Z.; Zhang, J.; Cheng, H.; Liu, G.; Park, G. T.; Cavallo, L.; Wang, L.; Alshareef, H. N.; Sun, Y. K.; Ming, J. Electrolyte-mediated stabilization of high-capacity micro-sized antimony anodes for potassium-ion batteries. *Adv. Mater.* **2021**, *33* (8), No. 2005993.
(21) Tan, H.; Du, X.; Zhou, R.; Hou, Z.; Zhang, B. Rational design of microstructure and interphase enables high-capacity and long-life carbon anodes for potassium ion batteries. *Carbon* **2021**, *176*, 383−389.
(22) Du, X.; Gao, Y.; Zhang, B. Building elastic solid electrolyte interphases for stabilizing microsized antimony anodes in potassium ion batteries. *Adv. Funct. Mater.* **2021**, *31* (26), No. 2102562.
(23) Jo, C. H.; Myung, S. T. Role of Ether-Based Electrolytes in Enhancing Potential of Potassium-ion Batteries. *Adv. Energy Mater.* **2024**, *14* (21), No. 2400217.
(24) Li, L.; Zhao, S.; Hu, Z.; Chou, S.-L.; Chen, J. Developing better ester-and ether-based electrolytes for potassium-ion batteries. *Chem. Sci.* **2021**, *12* (7), 2345−2356.
(25) Liu, S.; Mao, J.; Zhang, L.; Pang, W. K.; Du, A.; Guo, Z. Manipulating the solvation structure of nonflammable electrolyte and interface to enable unprecedented stability of graphite anodes beyond 2 years for safe potassium-ion batteries. *Adv. Mater.* **2021**, *33* (1), No. 2006313.
(26) Zhang, H.; Wang, H.; Li, W.; Wei, Y.; Wen, B.; Zhai, D.; Kang, F. Enabling High-Performance Potassium-Ion Batteries by Manipulating Interfacial Chemistry. *Adv. Funct. Mater.* **2024**, *34* (21), No. 2312368.
(27) Zhang, D.; Fu, H.; Ma, X.; Yu, X.; Li, F.; Zhou, J.; Lu, B. Nonflammable phosphate-based electrolyte for safe and stable potassium batteries enabled by optimized solvation effect. *Angew. Chem.* **2024**, *136* (29), No. e202405153.
(28) Fan, L.; Xie, H.; Hu, Y.; Caixiang, Z.; Rao, A. M.; Zhou, J.; Lu, B. A tailored electrolyte for safe and durable potassium ion batteries. *Energy Environ. Sci.* **2023**, *16* (1), 305−315.
(29) Liu, S.; Mao, J.; Zhang, Q.; Wang, Z.; Pang, W. K.; Zhang, L.; Du, A.; Sencadas, V.; Zhang, W.; Guo, Z. An intrinsically nonflammable electrolyte for high-performance potassium batteries. *Angew. Chem., Int. Ed.* **2020**, *59* (9), 3638−3644.
(30) Fickert, M.; Assebban, M.; Canet-Ferrer, J.; Abellan, G. Phonon properties and photo-thermal oxidation of micromechanically exfoliated antimonene nanosheets. *2D Mater.* **2021**, *8* (1), No. 015018.
(31) Park, S.-H.; King, P. J.; Tian, R.; Boland, C. S.; Coelho, J.; Zhang, C.; McBean, P.; McEvoy, N.; Kremer, M. P.; Daly, D.; et al. High areal capacity battery electrodes enabled by segregated nanotube networks. *Nat. Energy* **2019**, *4* (7), 560−567.
(32) Xu, K. *Electrolytes, Interfaces and Interphases: Fundamentals and Applications in Batteries*; Royal Society of Chemistry, 2023.
(33) Zhao, J.; Jagger, B.; Olbrich, L. F.; Ihli, J.; Dhir, S.; Zyskin, M.; Ma, X.; Pasta, M. Transport and thermodynamic properties of KFSI in TEP by operando raman gradient analysis. *ACS Energy Lett.* **2024**, *9* (4), 1537−1544.
(34) Goodenough, J. B.; Kim, Y. Challenges for rechargeable Li batteries. *Chem. Mater.* **2010**, *22* (3), 587−603.
(35) Lin, Y.; Yu, Z.; Yu, W.; Liao, S.-L.; Zhang, E.; Guo, X.; Huang, Z.; Chen, Y.; Qin, J.; Cui, Y.; Bao, Z. Impact of the fluorination degree of ether-based electrolyte solvents on Li-metal battery performance. *J. Mater. Chem. A* **2024**, *12* (5), 2986−2993.
(36) Gao, Y.; Li, W.; Ou, B.; Zhang, S.; Wang, H.; Hu, J.; Kang, F.; Zhai, D. A dilute fluorinated phosphate electrolyte enables 4.9 V-class potassium ion full batteries. *Adv. Funct. Mater.* **2023**, *33* (47), No. 2305829.
(37) Yu, S.; Kim, S. O.; Kim, H. S.; Choi, W. Computational screening of anode materials for potassium-ion batteries. *Int. J. Energy Res.* **2019**, *43* (13), 7646−7654.
(38) Kim, J. H.; Hyun, J. H.; Kim, S.; Park, W. H.; Yu, S. H. Phosphorus-Based Flame-Retardant Electrolytes for Lithium Batteries. *Adv. Energy Mater.* **2025**, *15*, No. 2500587.
(39) Yu, W.; Lin, K.-Y.; Boyle, D. T.; Tang, M. T.; Cui, Y.; Chen, Y.; Yu, Z.; Xu, R.; Lin, Y.; Feng, G.; et al. Electrochemical formation of

bis (fluorosulfonyl) imide-derived solid-electrolyte interphase at Li-metal potential. *Nat. Chem.* **2025**, *17*, 246−255.
(40) He, X.-D.; Liu, Z.-H.; Liao, J.-Y.; Ding, X.; Hu, Q.; Xiao, L.-N.; Wang, S.; Chen, C.-H. A three-dimensional macroporous antimony@carbon composite as a high-performance anode material for potassium-ion batteries. *J. Mater. Chem. A* **2019**, *7* (16), 9629−9637.
(41) Bo, Z.; Chen, P.; Zheng, Z.; Huang, Y.; Yan, J.; Cen, K.; Xu, Q.; Yang, H.; Ostrikov, K. Tightly-connected carbon-coated FeS2 hollow sphere-graphene microstructure for ultrafast and stable potassium ion storage. *J. Energy Storage* **2024**, *84*, No. 110984.
(42) Bo, Z.; Chen, P.; Huang, Y.; Zheng, Z.; Zhao, Y.; Yan, J.; Cen, K.; Shao, H.; Lin, Z.; Yang, H.; Ostrikov, K. K. Resolving the tradeoff between energy storage capacity and charge transfer kinetics of sulfur-doped carbon anodes for potassium ion batteries by pre-oxidation-anchored sulfurization. *Energy Storage Mater.* **2024**, *69*, No. 103393.
(43) Torres, I.; Alcaraz, M.; Sanchis-Gual, R.; Carrasco, J. A.; Fickert, M.; Assebban, M.; Gibaja, C.; Dolle, C.; Aldave, D. A.; Gómez-Navarro, C.; et al. Continuous-Flow Synthesis of High-Quality Few-Layer Antimonene Hexagons. *Adv. Funct. Mater.* **2021**, *31* (28), No. 2101616.
(44) Peng, L.; Ye, S.; Song, J.; Qu, J. Solution-phase synthesis of few-layer hexagonal antimonene nanosheets via anisotropic growth. *Angew. Chem., Int. Ed.* **2019**, *58* (29), 9891−9896.